



Combined Nd:YAG and Er:YAG lasers for real-time closed-loop tissue-specific laser osteotomy

HAMED ABBASI,^{1,6}  LINA M. BELTRÁN BERNAL,¹  ARSHAM HAMIDI,¹  ANTOINE DRONEAU,^{1,2}  FERDA CANBAZ,¹  RAPHAEL GUZMAN,³  STEVEN L. JACQUES,⁴  PHILIPPE C. CATTIN,⁵  AND AZHAR ZAM^{1,7} 

¹*Biomedical Laser and Optics Group (BLOG), Department of Biomedical Engineering, University of Basel, CH-4123 Allschwil, Switzerland*

²*Grenoble INP, Grenoble Alpes University, Phelma, France*

³*Department of Neurosurgery, University Hospital Basel, CH-4056 Basel, Switzerland*

⁴*Department of Bioengineering, University of Washington, Seattle, Washington 98195, USA*

⁵*Center for medical Image Analysis and Navigation (CIAN), Department of Biomedical Engineering, University of Basel, CH-4123 Allschwil, Switzerland*

⁶*hamed.abbasi@unibas.ch*

⁷*azhar.zam@unibas.ch*

Abstract: A novel real-time and non-destructive method for differentiating soft from hard tissue in laser osteotomy has been introduced and tested in a closed-loop fashion. Two laser beams were combined: a low energy frequency-doubled nanosecond Nd:YAG for detecting the type of tissue, and a high energy microsecond Er:YAG for ablating bone. The working principle is based on adjusting the energy of the Nd:YAG laser until it is low enough to create a microplasma in the hard tissue only (different energies are required to create plasma in different tissue types). Analyzing the light emitted from the generated microplasma enables real-time feedback to a shutter that prevents the Er:YAG laser from ablating the soft tissue.

© 2020 Optical Society of America under the terms of the [OSA Open Access Publishing Agreement](#)

1. Introduction

Due to the many side effects of the traditional osteotomy tools, e.g., poor surface evenness, mechanical vibrations, high amount of heat production, limited cutting geometry, high material loss, and potential contamination, alternative solutions are sought. Lasers seem to be a perfect candidate for replacing conventional saws and drills in osteotomy procedures [1–11]. However, lasers pose the risk of collateral damage to the neighboring tissue if feedback about the type of tissue is not provided. In order to preserve the adjacent soft tissue, several approaches to such differentiation have been developed using the optical properties of the ablated tissues. These methods include optical coherence tomography (OCT) [12,13], Raman spectroscopy [14–17], autofluorescence spectroscopy [18,19], diffuse reflectance spectroscopy (DRS) [20–23], ablative optoacoustic techniques [24–29], random lasing [30], laser-induced breakdown spectroscopy (LIBS) [31–42], and combustion/pyrolysis light analysis [43,44]. However, many of these methods have not been tested in combination with an ablating laser; studies have focused on tissue differentiation only. In addition to the work carried out in the area of tissue-specific surgery, several studies have used similar approaches for detecting cancer borders during surgery [45–51]. Each method has its own advantages and disadvantages. Some of them, like OCT and Raman, use a low power continuous wave (CW) laser, where the diagnostic beam does not involve ablation. Other methods, like ablative optoacoustic techniques, require high energy pulsed lasers to produce a measurable acoustic wave. However, the required energy levels can create damage

to sensitive tissues with just one pulse. LIBS also has the potential to differentiate tissue types (not only between hard and soft tissues, but also between different soft tissues) and, additionally, to provide feedback regarding laser-induced thermal damage (dehydration [39] and carbonization [38]). However, during surgery, at least a single shot of the laser (around tens of millijoules using nanosecond pulses) needs to be applied to the tissue in order to detect its type. Therefore, in both LIBS and acoustic methods, the applied energy could ablate a small amount of the tissue. Raman spectroscopy, another advanced optical technique, can provide information regarding the molecular bonds of the tissue. However, due to its low cross-section, a few seconds of integration of the measured signal are required [14,15], which makes it unsuitable as a real-time feedback sensor. Photodiode-based pyrolysis analysis (also known as combustion analysis) is yet another method to achieve tissue-specific cutting during microsecond Er:YAG osteotomy [43,44]. Here,

Table 1. A comparison of optical sensor-based laser ablation published works for tissue-specific cutting

| Work | method | Ablating laser | Diagnostic light source | Ablation-free detection ^a | Real-time ^b | Closed-loop ^c |
|---------|-------------------------------------|--------------------------------------|-----------------------------------|--------------------------------------|------------------------|--------------------------|
| [12] | OCT | N.A. ^d | Swept source (1060 nm) | ✓ | ✗ | ✗ |
| [14–17] | Raman | N.A. | CW (785 nm) | ✓ | ✗ | ✗ |
| [18] | Autofluorescence | N.A. | mercury lamp | ✓ | ✗ | ✗ |
| [20–23] | Diffuse Reflectance | N.A. | Pulsed Xenon/ Halogen lamp | ✓ | ✗ | ✗ |
| [24–26] | Shockwave (speckle-analysis) | ns-Nd:YAG (1064 nm) | CW Nd:YAG (532 nm) ^e | ✗ | ✗ | ✗ |
| [27,28] | Shockwave (Mach-Zehnder) | ns-Nd:YAG (532 nm) | Same as ablating one | ✗ | ✗ | ✗ |
| [29] | Ablative optoacoustic (FBG) | ms-fiber laser (1070 nm) | Same as ablating one | ✗ | ✗ | ✗ |
| [30] | Random lasing | ns-Nd:YAG (532 nm) | Lasing by the tissue ^f | ✗ | ✗ | ✗ |
| [31–39] | ns-LIBS | ns-Nd:YAG /Excimer (1064/532/193 nm) | Same as ablating one | ✗ | ✗ | ✗ |
| [40] | Double-pulse LIBS | μs-Er:YAG (2940 nm) | ns-Nd:YAG (532 nm) | ✗ | ✗ | ✗ |
| [41] | CO ₂ -LIBS | Pulsed CO ₂ (10.6 μm) | Same as ablating one | ✗ | ✓ | ✗ |
| [42] | fs-LIBS | fs-mode-locked (1030 nm) | Same as ablating one | ✗ | ✓ | ✗ |
| [43,44] | Photodiode-based pyrolysis analysis | μs-Er:YAG (2940 nm) | Same as ablating one | ✗ | ✓ | ✓ |

^aThis column shows whether detection can be provided without ablating the tissue which meant to be preserved.

^bReal-time here means diagnosis within millisecond range. Some works with near-real-time analysis (more than a second processing time) were not marked as real-time in this table.

^cOnly those works in which the feedback from the dedicated sensor was sent to the ablating laser/shutter (in order to stop cutting) were marked as closed-loop, here. Works with closed-loop ability without testing or a concept as a future plan were not marked in this table.

^dN.A. in this column means that in the published work, only the ability of the method for tissue differentiation was examined and it was not combined with any ablating laser.

^eIn speckle analysis, the ablation caused during the procedure required to determine the type of tissue is caused by the high energy laser used to generate shockwave at the tissue.

^fIn random lasing, the ablation caused during the procedure required to determine the type of tissue is caused by the high energy laser used to pump the tissue for lasing.

a photodiode is used to observe the light emitted from the pyrolysis created in the ablation zone. The pyrolysis light is observable only at high energy densities. In this setup, no additional laser is utilized. Employing a single laser to both ablate and differentiate tissue offers a simpler optical setup. However, if the laser beam reaches a tissue that should be preserved, the laser beam would be stopped, as a result, the tissue-type diagnosis cannot be continued (i.e., no ablation beam, no diagnosis beam).

Table 1 provides a summary comparing studies where different methods were used to differentiate tissues. The last three columns of the table are dedicated to comparing three important features of a feedback mechanism that are required for an applicable system. These are having a non-ablating diagnostic laser, functioning in real-time, and tested together within a closed-loop setup. Each feature is more precisely defined in the table's footnote. The middle column shows whether two different lasers are used for ablation and differentiation or not. Table 1 covers all studies, to the best of our knowledge, related to tissue-specific surgeries. However, the table does not cover works that have used a similar feedback mechanism for detecting cancer margins [45–51] in the tissues.

As shown in Table 1, previously conducted works could not completely fulfill the requirement for a closed-loop smart laser osteotomy. Therefore, the current study is intended to fulfill all requirements. The current study introduces a different approach, whereby ablation is performed in hard tissues only, and no ablation occurs in soft tissue. We tested this approach in a real-time closed-loop scenario. Two laser beams were combined: a high energy Er:YAG for ablating the bone and a low energy Nd:YAG for detecting the type of tissue. Therefore, when the beam encounters soft tissue, only the Er:YAG beam is blocked (using a fast mechanical shutter), and tissue-type differentiation can continue. The energy of the Nd:YAG laser required is low enough to be delivered using fiber optics, making it more suitable for miniaturization for minimally-invasive surgery (MIS).

2. Methodology

2.1. Hard tissue ablation process

Bone ablation can be performed in different ways, e.g., by photothermal or electro-mechanical means. Photothermal ablation has shown excellent results. It is based on the high absorption of water and mineral components (e.g., hydroxyapatite) at mid-infrared wavelengths, like 3 μm and 10 μm , for lasers working in the microsecond regime [2,3,52–55]. Once the microsecond laser pulse strikes the bone surface, it heats up the water molecules accumulated in the interstitial walls of the bone. High pressure (hundreds of bars) is created inside the bone structure, leading to explosive evaporation of the tissue [55]. The most common lasers used for tissue ablation are Ho:YAG at 2.1 μm , Er,Cr:YSGG at 2.79 μm , Er:YAG at 2.94 μm and CO₂ at 9.3, 9.6, and 10.6 μm [56–58]. The Er:YAG laser causes minimal damage to the bone surroundings [59,60]. To ensure efficient tissue ablation with less collateral damage and faster healing time, the stability of the laser pulses [61] and the highest degree of absorption are desirable. In this study, a flashlamp-pumped Er:YAG laser (LiteTouch by Syneron) with microsecond-long pulses was used to ablate the bone.

2.2. Tissue differentiation working principle

Depending on the applied energy and pulse duration of a laser, several different phenomena may occur when the laser interacts with biological tissues [62–64]. When tissue interacts with pulsed lasers, there might be a nonlinear absorption of the light, thus, the type of interaction can be changed quickly by changing the parameters of the laser [65]. A laser-tissue interaction map can explain the underlying principle of the work. The laser-tissue interaction map was initially depicted by Boulnois in 1986 [66]. Later, the map was reproduced and modified on different

occasions by other researchers [55,67–69]. Due to limited access to ultra-short laser pulses, the initial map included four main phenomena: (I) photochemical (mainly only for CW lasers), (II) thermal (including coagulation, vaporization, carbonization, and melting), (III) photoablative, and (IV) electro-mechanical. Basically, the different phenomena are the result of laser energy converting to different kinds of energy: chemical, thermal, or mechanical [70]. In most of the recently reproduced maps, the electro-mechanical part (using short and ultra-short laser pulses only) is divided into two different sections: photodisruption and plasma-induced ablation (there is no consensus for that, and other terms are also used). However, in both cases (photodisruption and plasma-induced ablation), the tissue is ionized and a localized plasma is produced at the ablation zone (breakdown). The difference is the higher impact of mechanical effects in photodisruption (the term disruption originates from the Latin word *ruptus*, meaning ruptured) [69]. Mechanical effects produce shockwaves (high pressure gradients moving at supersonic speed at the shock front) in all tissues, cavitation (explosive vaporization involving negative tensile waves that disrupt a material, causing successive expansion and collapse due to strong compression of water and carbon oxides) in soft tissues, and jet formation (only in fluids) near a solid boundary during collapse from cavitation [71,72]. Figure 1 shows a representation of the laser-interaction map from [69].

Which interaction mechanism tissue undergoes depends on multiple laser parameters; these include pulse duration and applied power density as the two main parameters as used in the two-dimensional map. Moreover, tissue properties like transmission, reflection, scattering, absorption (function of laser wavelength), tissue density, heat conduction and heat capacity also determine the type of interaction. A variety of optical and mechanical properties of different kinds of tissue widen the borders shown in Fig. 1. This means that a specific laser parameter can lead to two different interactions for different tissues. The optical breakdown formed by nanosecond pulses is always associated with a shock wave (for both hard and soft tissues) and cavitation (only for soft tissues) even at the very threshold. In electro-mechanical ablation relatively powerful thermoelastic tensile pressure is generated, which can produce cavitation inside the irradiated medium; its amplitude is a function of the absorption coefficient of the medium and the power density of the applied laser beam [73]. Considering all the differences between the mechanical and physical properties of hard and soft tissues, the fact that cavitation (negative tensile pressure disruption) occurs only in soft tissues, and that up to one fourth of the applied energy will be consumed in cavitation [69], at specific pulse durations, higher energy is required to start the breakdown at soft tissues (different required dosimetry based on the tissue optics [74]). The critical point determined in Fig. 1 (the single red dot) shows the starting point or threshold of bone ablation for a nanosecond Nd:YAG laser.

Due to the complexity of all involved parameters, no complete model has been formulated to describe the ablation process. However, two simplified models are useful for describing the working principle utilized in the current study: “steady-state” and “blow-off”. The former is normally used to describe longer pulses (typically in the microsecond regime) as compared to the later one (typically shorter than 100 ns) [62]. Both models seek an ablation threshold, $\Phi_{\text{threshold}}$ [J/cm^2], in which only an energy density (radiant exposure) higher than the ablation threshold can onset the ablation. Molecular dynamic simulations have confirmed that lower energy density will result in heating the tissue without material ejection; this has been confirmed by some experiments as well [75].

The steady-state model is based on the assumption of having constant ablation enthalpy (also known as the heat of ablation), H [J/kg]. In this model, the ablation efficiency, η [kg/J], i.e., the amount of mass removed per unit energy, is related to the applied energy density, Φ_{applied} [J/cm^2], using the following equation:

$$\eta = \frac{\Phi_{\text{applied}} - \Phi_{\text{threshold}}}{H\Phi_{\text{applied}}} \quad (1)$$

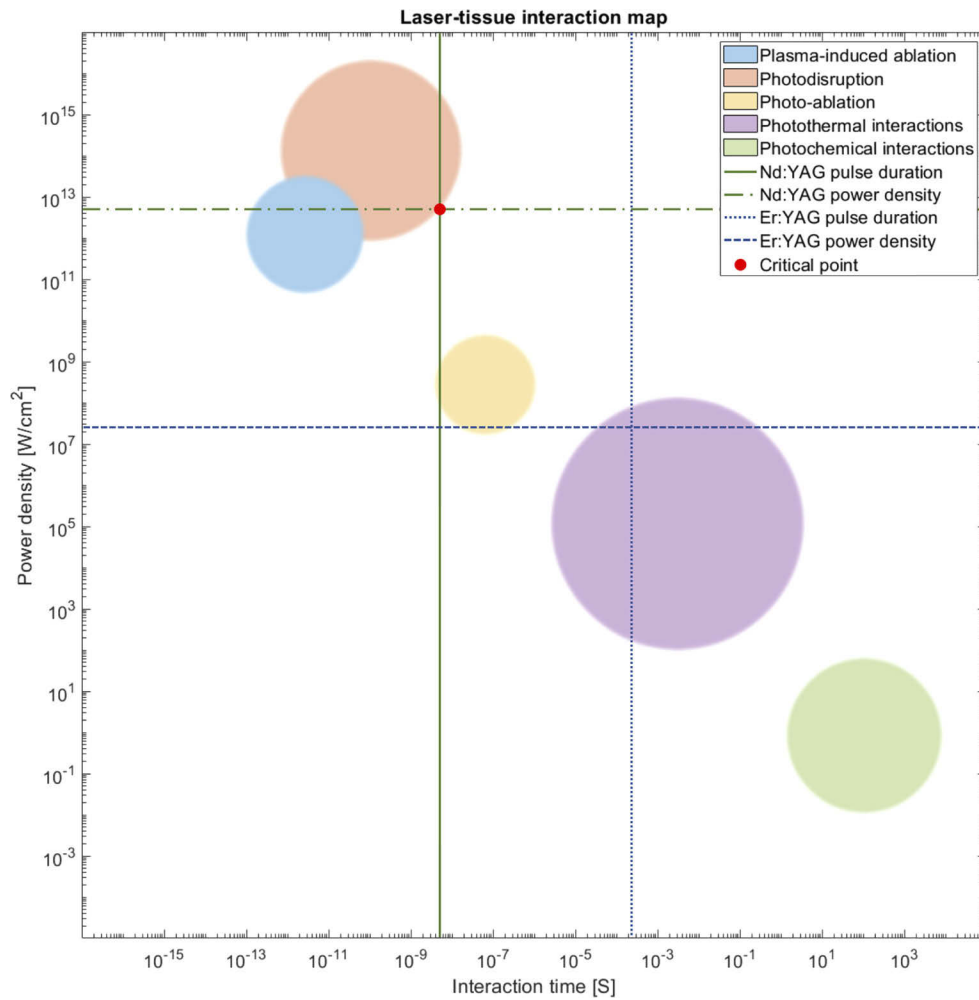


Fig. 1. Laser-tissue interaction map. The vertical blue dotted and the horizontal blue dashed lines show the pulse duration and power density of the Er:YAG laser that were used in the experiments. The red dot on the map (critical point) shows where the vertical green solid (Nd:YAG pulse duration), and horizontal green dash-dotted (Nd:YAG power density) lines meet. This critical point is the starting point of ablation, which varies from hard to soft tissues.

The blow-off model, which is based on the satisfaction of the Beer-Lambert law for the spatial distribution of the absorbed energy, can be described by the following equation:

$$\eta = \frac{\rho}{\mu\Phi_{applied}} \ln \left(\frac{\Phi_{applied}}{\Phi_{threshold}} \right) \quad (2)$$

where ρ [kg/m³] is tissue density, and μ [cm⁻¹] is the absorption coefficient of tissue at the applied wavelength. In both models, the ablation efficiency would be zero (no ablation) if the applied energy density does not exceed the ablation threshold ($\Phi_{applied} \leq \Phi_{threshold}$).

2.3. Specimens

In this experiment, five different bisected pig femur slices were bought from a local supermarket; two of them were used to train the shutter, and the rest were used for testing. All specimens were washed using tap water right before the experiment, in order to remove possible pollution at the surface of the specimens. Both sides of each bisected slice were used, therefore, four series of data were recorded to train the shutter, and six experiments were carried out for testing. Each specimen consisted of four different kinds of tissue: the hard tissue bone and the soft tissues bone marrow, muscle and fat. By moving the specimens using a motorized translation stage, the laser beam encountered different tissue types on each trip. Since the specimens used were available as food-based material, ethical committee approval was not required.

2.4. Experimental setup

Two laser beams were combined to perform ablation and tissue differentiation, a microsecond Er:YAG and a nanosecond Nd:YAG, respectively. The Er:YAG laser energy was 226 mJ (measured by PE50-DIF-ER-C pyroelectric energy meter, Ophir, USA), with a pulse duration of 106.4 μ s (measured by PDA20H-EC - PbSe fixed gain pre-amplified detector, Thorlabs, USA, connected to an IR bandpass filter, FB3000-500, Thorlabs, USA), and Fluke 190-504 scope meter, Fluke Corporation, USA), and emitting a 2940 nm Mid-Infrared (MIR) beam. Note that lower energies could also be used for performing photothermal bone ablation; however, it might result in lower ablation efficiency. Also, it is worth mentioning that shorter pulse durations matching thermal relaxation time of bone (typically below 80 μ s [76]) would be desirable, if accessible. The frequency-doubled Q-switched Nd:YAG laser energy was 4.10 mJ (measured by EnergyMax-USB J-50MB-YAG Energy Sensor, Coherent, USA), with a pulse duration of 5 ns, and emitting a 532 nm green beam (numbers provided by the manufacturing company, Quantel, France). The energy of both lasers was measured after the beams passed through all optical components. The experimental setup is shown in Fig. 2. The Er:YAG laser is placed out of the frame at the left side and its beam path is depicted in red. The Er:YAG beam was divided into two unequal parts using a microscope slide (part (a) in Fig. 2). Around 4% of the light reflected to the photodiode (part (b) in Fig. 2) was used for synchronization while the rest of the light was transmitted through the microscope slide and then directed to the specimen. The Nd:YAG laser is also placed out of the frame in Fig. 2 on the right, and its path beam is depicted in green. Two beams were combined using a dichroic mirror (Er:YAG in reflection mode, and Nd:YAG in transmission mode), shown as (d) in Fig. 2. The combined beam was passed through a broadband convex lens with a focal length of 2 cm (part (e) in Fig. 2) in order to focus the beam at the surface of the specimens. It is worth mentioning that during tissue ablation (especially for soft tissues) with such a short focal length lens, the lens can become dirty with debris (water and small fatty particles ablated from the soft tissue) hitting the lens surface. If the focal length were longer, different laser beams could focus on two different points, especially if the wavelength and quality of the beams are not similar.

To calculate the focal spot size of each laser beam at the specimen's surface, Gaussian optics were used, taking into account the initial beam size and the beam quality factor, M-squared (M^2), also known as the focusability factor. This parameter allows us to determine the extent of beam divergence compared to an ideal Gaussian beam, which has the same beam size but $M^2=1$. Therefore, beam divergence (θ) for a real Gaussian beam is defined as

$$\theta = M^2 \frac{\lambda}{\pi w_0}. \quad (3)$$

Here, w_0 and λ indicate the beam radius of the laser at its waist position and the center wavelength of the laser, respectively. The M^2 of the beam allows one to determine the beam propagation of the real Gaussian and, therefore, the actual beam size at any position in its trajectory. In our case,

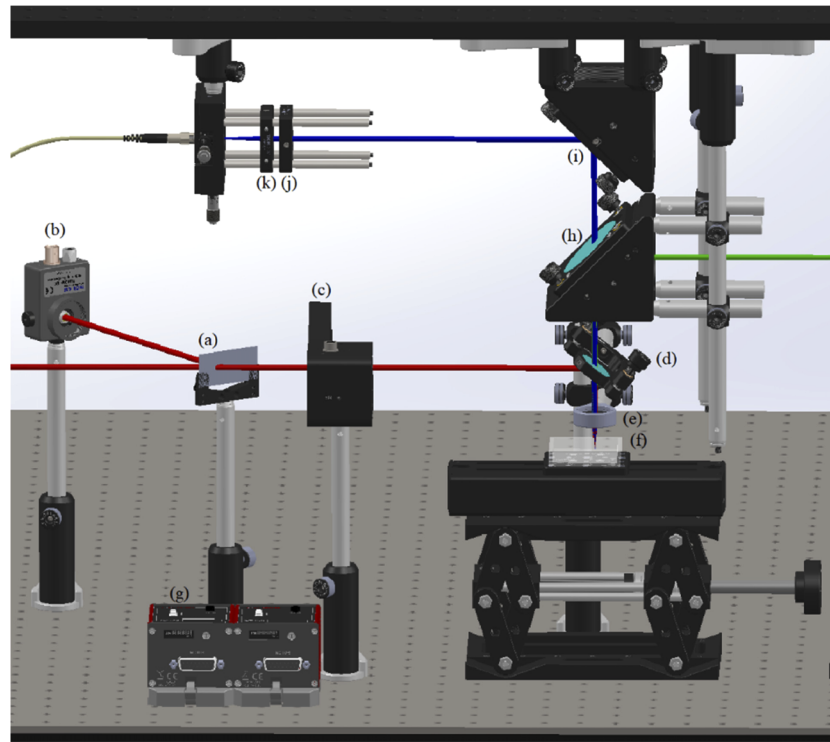


Fig. 2. The CAD design of the experimental setup (performed in SolidWorks 2017). (a): microscope slide as beam splitter, (b): photodiode, (c): shutter, (d): 1st dichroic mirror, (e): focusing lens, (f): sample holder and translation stage, (g): controller of shutter and translation stage, (h): 2nd dichroic mirror, (i): broadband mirror, (j): notch filter, (k): focusing lens. The path of Er:YAG, Nd:YAG, and collected plasma light is depicted in red, green, and dark blue, respectively. The yellow optical fiber depicted in the left side of the figure, guides the light to the camera. The wires for connecting the photodiode, translation stage, shutter, lasers and camera were removed from the figure, intentionally, to avoid a crowded design.

we are interested in knowing the beam size at the focal point, where the tissues are positioned for ablation. The initial beam size and M^2 of the Nd:YAG laser were provided by the manufacturing company as 6.5 mm and ≤ 2 , respectively. We experimentally measured initial beam size and M^2 of the Er:YAG laser. The beam size was estimated by using the knife-edge method, in which the beam is cut axially at different positions. We started covering the beam slowly in the axial plane so that the power went from maximum to minimum as we covered almost all of the beam with the blade. Afterwards, we applied the equations explained in [77] to fit the power function. Then, we obtained the beam size at the focal plane. Since the laser beam can also ablate the blade at the focus point, we did not put the blade there. Instead, we used a lens to focus the beam slowly so that we performed the knife-edge method at approximately ten different positions along the propagation direction. Therefore, we determined the beam size at any position of its trajectory, including the focal plane. With information about all beam sizes along its propagation, the beam diameter (d) can be fitted as a function of the propagation direction (z) by using a hyperbolic function [78]

$$d(z) = \sqrt{A + Bz + Cz^2} \quad (4)$$

where A, B, and C are the fitting parameters. Accordingly, M^2 can be determined from

$$M^2 = \frac{\pi}{8\lambda} \sqrt{4AC - B^2}. \quad (5)$$

We evaluated the beam quality factor of the Er:YAG laser to be ~ 22 . Using this information, we estimated the beam size at the surface of the tissue to be $\theta_{Er:YAG} = 103.35 \mu\text{m}$ and $\theta_{Nd:YAG} = 4.17 \mu\text{m}$. The variation between the calculated spot sizes is due to the difference between the M^2 of the lasers as well as their wavelengths. The actual spot sizes might be slightly different as compared to the estimated ones, due to any possible imperfection in the utilized focusing system. In the experiments, the Er:YAG and the Nd:YAG lasers operated at 20 Hz and 4 Hz, respectively, to ablate and determine the type of tissue. In other words, after every five Er:YAG pulses applied to the specimens, the tissue type was determined by an Nd:YAG laser pulse. The sample was located on top of a motorized translation stage connected to a direct-drive servo motor with a 50 mm travel range (DDSM50/M, Thorlabs, USA). The translation stage (part (f) in Fig. 2) moved at a speed of 1 mm/s for 7 runs for each specimen. At this speed, specimens were subject to one Er:YAG pulse every 50 μm and one Nd:YAG shot every 250 μm (see Fig. 3). This speed leads to one Er:YAG shot every 50 μm , and one Nd:YAG shot every 250 μm (see Fig. 3). As mentioned above, the Nd:YAG laser generated a localized low-energy microplasma at the surface of the bone. The microplasma was collected using the same lens used for focusing and, then, passed through a dichroic mirror reflecting 532 nm and transmitting almost the rest of the visible spectrum towards the collection part (parts (i), (j) and (k) in Fig. 2). The path of the collected plasma light is depicted in Fig. 2 with a dark blue line. After passing the dichroic mirror, the collected light is transmitted through the second dichroic mirror (part (h) in Fig. 2) that was used to reflect the Nd:YAG beam. Then, the collected light is directed (by part (i) in Fig. 2) to the multi-mode optical fiber for delivery to the camera.

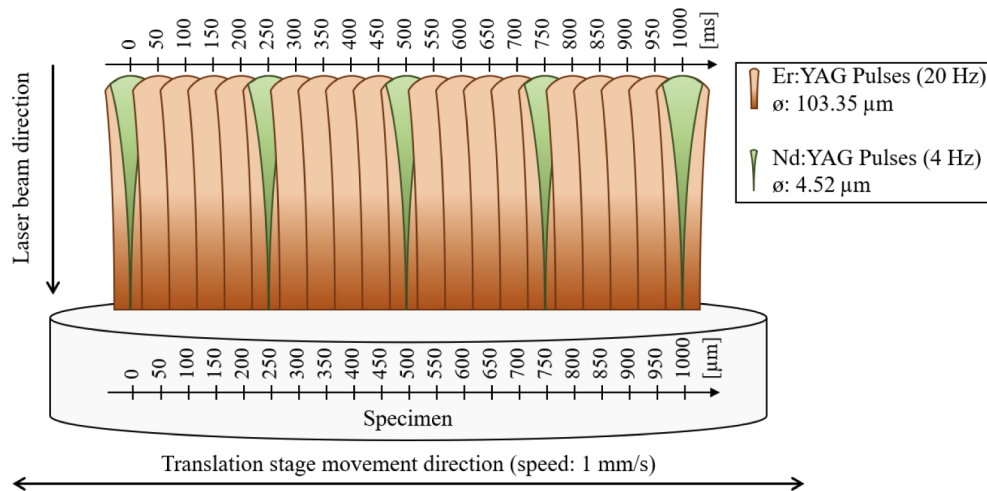


Fig. 3. Schematic of Er:YAG and Nd:YAG beam scales on the surface of the specimens. Time and space scales are positioned at the top and the bottom, respectively. It shows the relative frequency and distance of the ablation (Er:YAG laser) and tissue differentiation (Nd:YAG laser).

The collection part includes a notch filter with an optical density of 7 to avoid collecting reflections from the specimen; a collector lens; and an optical fiber (parts (j) and (k) in Fig. 2). The optical fiber directed the light to the camera (PI-MAX 4, Princeton Instruments, USA). A motorized shutter (SH1/M, Thorlabs, USA) can be seen in part (c) in Fig. 2, in the path of the

Er:YAG laser, which was commanded by the feedback signal received from the camera in a closed-loop and in a way to prevent cutting soft tissues. The Er:YAG laser used in the experiment could not be triggered externally, therefore, the first Er:YAG laser shots were blocked by the shutter as the shutter was programmed to start in closed mode only. In this way, first the Nd:YAG beam (tissue differentiation beam) probes the specimen, then the Er:YAG beam (cutting beam). In the end, an in-house swept-source OCT (SS-OCT) system was employed to observe the width and depth of the cuts. The SS-OCT system operated at a central wavelength of 1060 nm, a bandwidth of 100 nm, and a sweep rate of 100 kHz. The utilized SS-OCT system could provide 3 volumes per second with sizes up to 15.6 mm × 15.6 mm × 3.6 mm. The corresponding lateral and axial resolutions were 44 μm and 10 μm, respectively.

3. Results

3.1. Synchronization

To ensure sequential pulses for tissue differentiation and cutting, respectively, two laser beams and the camera were synchronized using TTL trigger pulses. Figure 4 shows the synchronization diagram of the connected devices. Synchronization started with the Er:YAG laser, as it could not be triggered externally. However, the first pulses of the Er:YAG were blocked to allow the Nd:YAG beam to reach the specimen first. When the photodiode receives a small portion of the Er:YAG beam, the photodiode generates a TTL trigger pulse (rise time (0 - 63%) equal to 35 μs), which is sent to the flash lamp input of the Nd:YAG laser. The flash lamp of the Nd:YAG laser (with a duration of 171.2 μs) excites the crystal rod of the laser, allowing the laser's Q-switch to open based on a pre-defined delay set by the user; the longer the delay, the lower the energy. Then, the Q-switch produces a TTL trigger pulse (with a duration of 25.6 μs), which is sent to the camera. The camera was controlled using LabVIEW. The translation stage started to move after the first trigger pulse from the Nd:YAG's Q-switch was received by the camera, and it stopped moving after 3.5 round trips (each round trip was equal to 100 mm). Around 80 ns after opening the Q-switch (information was provided by the manufacturing company), the Nd:YAG emits a pulse lasting 5 ns. Based on the applied energy and also the targeted material, the plasma expansion dynamics can vary [79,80]. Since the plasma generated in the current study had very low energy (4.1 mJ), it quenched quickly. Therefore, a short delay was applied to open the camera gate (200 ns after Q-switch triggering signal was received, i.e., 120 ns after lasing). The camera gate remained open for 4 ms and then closed before the next laser pulse arrived.

3.2. Training the shutter

As mentioned in Section 2.3, two of the five specimens were dedicated to training the shutter. Figure 5 shows the results of the training. One hundred data samples were recorded on each side of the training specimens for each tissue type in order to define a threshold for determining if ablation had occurred or not. The results confirmed that no ablation occurred at soft tissues.

3.3. Closed-loop results

After using two specimens to train the shutter to close upon reaching soft tissue, the experiment was carried out on the remaining three test specimens. Both sides of each specimen were subjected to the ablation setup developed, including and excluding the tissue differentiation setup. Figure 6 shows the results of the closed-loop experiment. The line cuts with the tissue differentiation setup in the loop are marked with a green box and those without tissue differentiation feedback are indicated with a red box. Figure 6(a)–(f) clearly shows that soft tissues were ablated only when tissue differentiation was shut off whereas bone was always ablated. The localized collateral thermal damages seen in some sections of the ablated bone samples are because the current

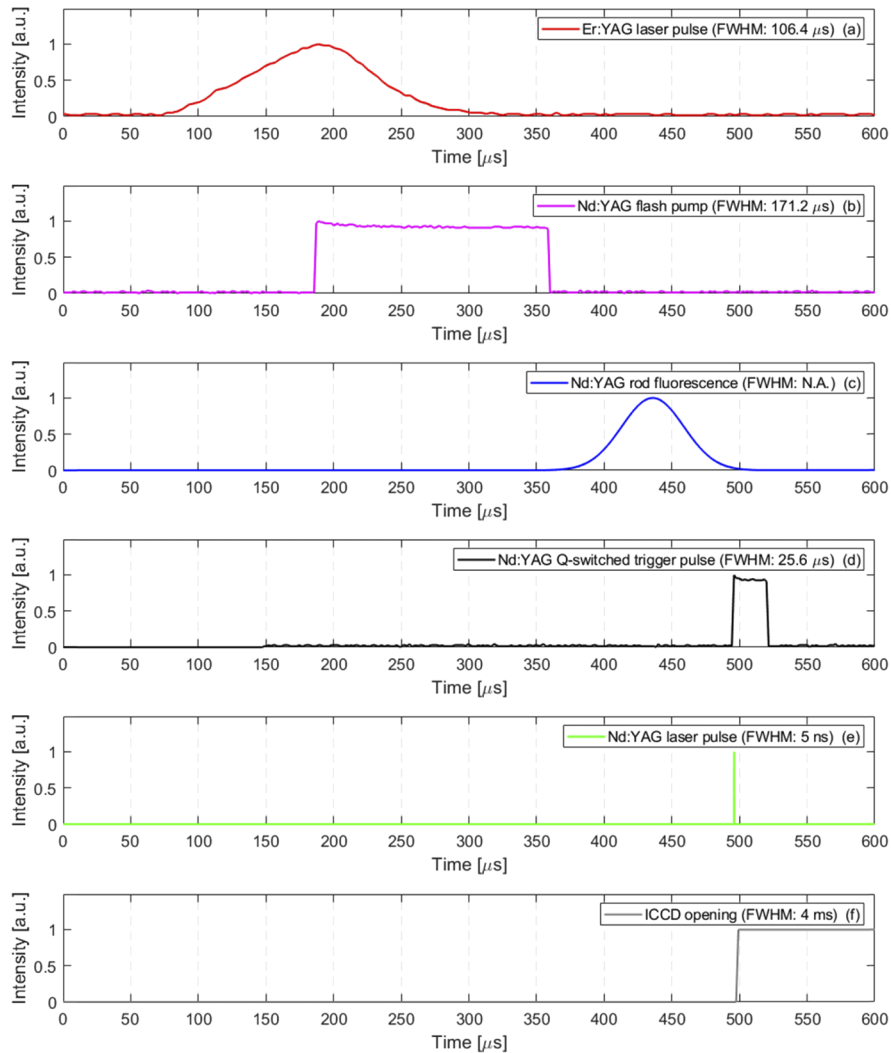


Fig. 4. The synchronization diagram of the connected devices in chronological order. Parts (a), (b), and (d) were recorded by a digital oscilloscope; parts (c), (e), and (f) were depicted by the authors based on the data received from the manufacturing companies. Based on the data provided by the camera, the shutter can be opened or closed (rising/falling time: 10 ms).

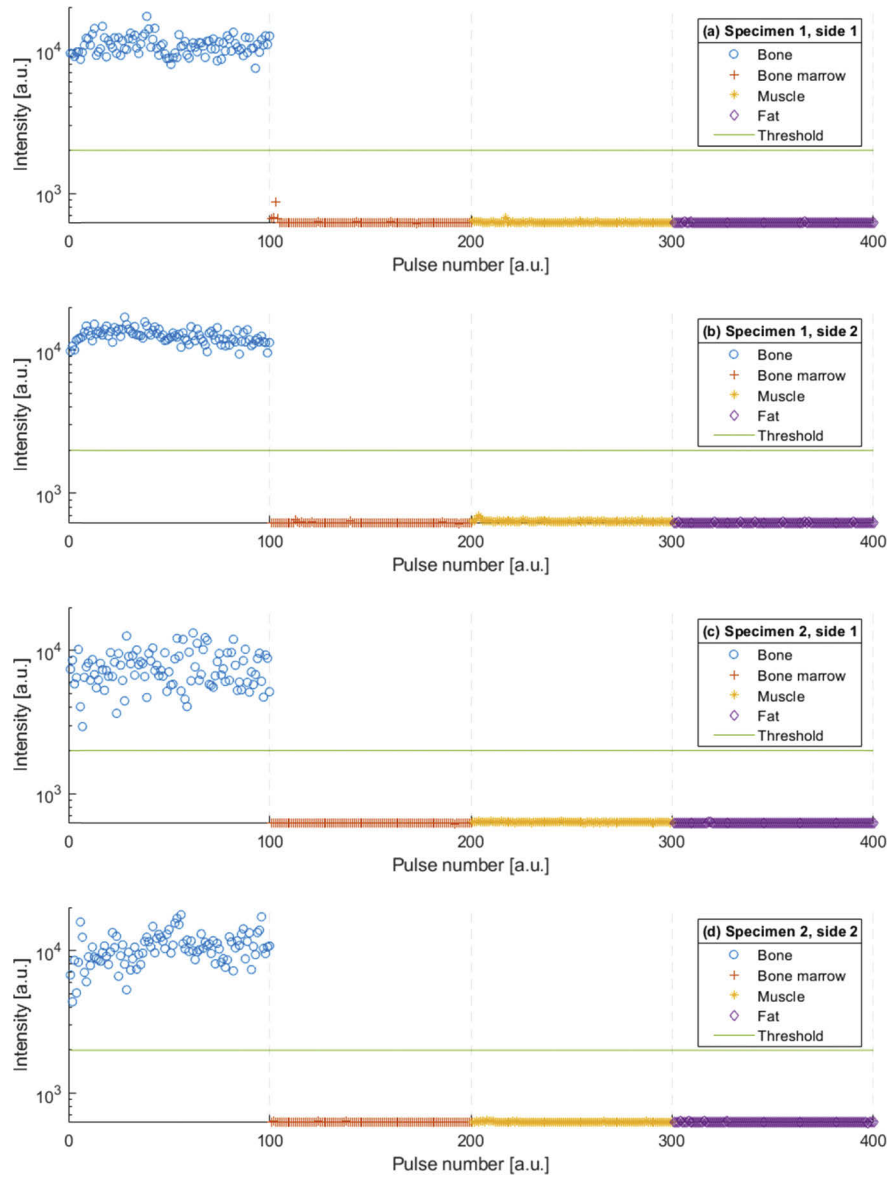


Fig. 5. Results from the training of the shutter. One hundred data points were recorded per tissue type, per specimen, per side (in total, four hundred times per tissue type). The result clearly confirms that ablation occurred only at hard tissue.

study did not use any irrigation; therefore, an irrigation system needs to be added to the current experimental setup to avoid carbonization [81,82].

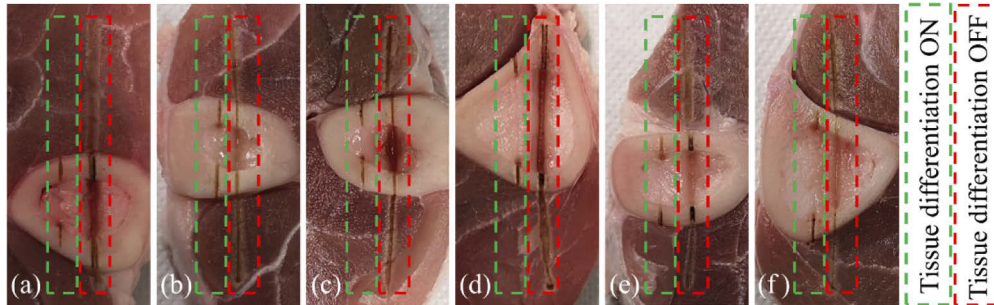


Fig. 6. (a)–(f) The results of the closed-loop experiment. All types of soft tissues were preserved when the real-time feedback system was ON. The photographs were taken after the experiment when the tissues were no longer fresh; this accounts for the observable detachment between bone and muscle in the figures.

3.4. OCT measurement

After the ablation experiments, the SS-OCT system was used to observe the profile of the cuts with and without the tissue differentiation system. Figure 7 shows the OCT images of the first specimen. The top view (en-face) is shown in Fig. 7(a); the three horizontal lines in bone marrow, bone, and muscle areas are marked as dashed lines in the image. A cross-section image (B-scan) of bone marrow, bone, and muscle are shown in Figs. 7(b), (c), and (d), respectively. In Figs. 7(b) and (d), where the tissue was supposed to be preserved, no cut is observable when the tissue differentiation system was ON (green box). In the red box (tissue differentiation OFF), the bone marrow was cut to a depth of 2.40 mm, and a width of 1.28 mm; muscle was cut to a depth and width of 0.62 mm and 1.21 mm, respectively. The widths were measured at the full width at half maximum (FWHM) of the cut. The data shows a higher ablation rate for the bone marrow as compared to muscle. In Fig. 7(c), the cut profile of bone in both scenarios (ON and OFF) is visible. In ON mode, the bone was cut to a depth and width of 1.47 mm and 0.28 mm, respectively; in OFF mode the bone was cut to a similar width (0.27 mm), but to a lower depth of 0.66 mm. In ON mode, where the Er:YAG beam ablated only the hard tissue, no debris from soft tissue was created. In OFF mode, where the beam ablated both hard and soft tissue, a high degree of debris was scattered (sprayed) on the lens surface. Such debris can pollute the focusing lens surface, especially if the lens is close to the sample surface (2 cm distance in our experiment). This debris can absorb some of the lasers' energy, especially that of the Er:YAG laser, which has a high absorption rate in water. Therefore, lower ablation efficiency was achieved in OFF mode, when the lens was covered by a superficial layer of watery/fatty particles. To avoid this, either a higher focal length should be chosen for the focusing lens or a hydrophobic protecting window should be added to the setup.

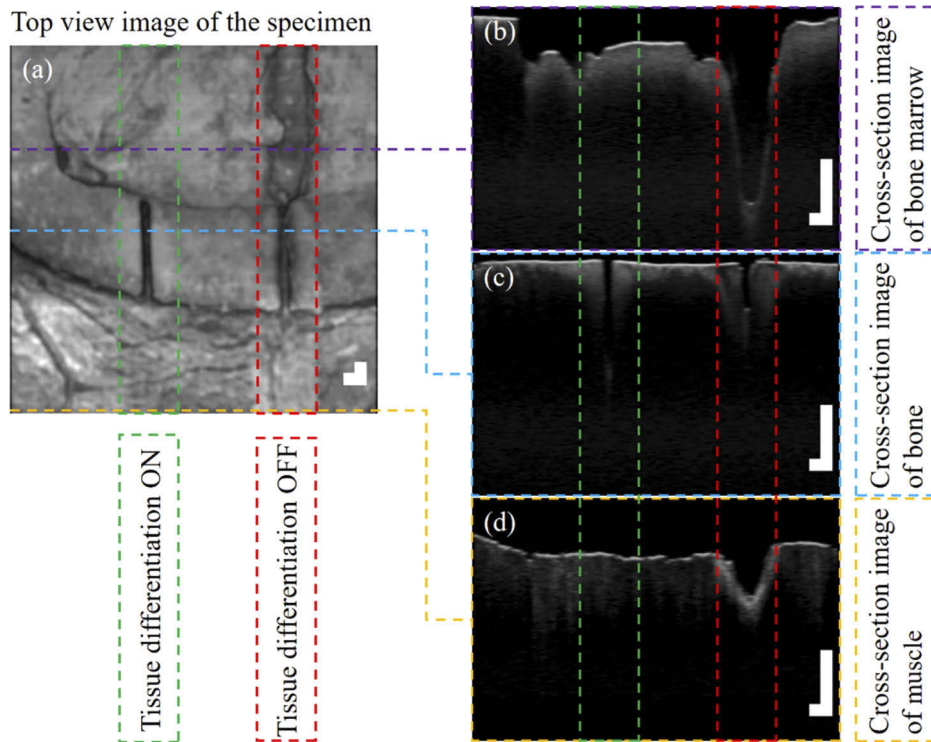


Fig. 7. OCT image of the first specimen with and without tissue differentiation in the loop. (a): top view of the cut (en-face). (b), (c), and (d): cross-section images (B-scan) of lines in bone marrow, bone, and muscle, respectively. The scale bar shown on the lower right side of each image is 1 mm in both vertical and horizontal planes. The non-symmetry of the scale bar in cross-section images is due to the difference between the lateral and axial resolution of the employed OCT system. OCT images were analyzed by ImageJ software.

4. Discussion

4.1. Advantage and disadvantage of the introduced method

Compared to other methods developed for tissue differentiation in laser surgery, the proposed method has several advantages. Similar to LIBS and laser-induced shockwave measurement methods, the procedure is based on generating plasma at the local spot of the tissue. However, in our method, the laser energy applied (4.10 mJ) is much lower than that used for LIBS (38 mJ for ns-Excimer laser [32,33], 73–108 mJ for ns-Nd:YAG laser [31,34–38], and 75–200 mJ for CO₂-LIBS [41]) or shockwave measurements (200 mJ for ns-Nd:YAG [27,28], and 0.75–15 J for ms-fiber laser [29]). Also, the energy applied is well below the reported energy required to pump the tissue for random lasing (100 mJ for ns-Nd:YAG [30]), and pyrolysis analysis (300–2000 mJ for μ s-Er:YAG [43,44]), which occurs inside the ablation zone in the laser-tissue interaction map. Differentiating tissue using a low energy (non-ablating) laser beam has two main advantages. First, it does not ablate the tissue that needs to be preserved (no probed ablation in soft tissues). Second, the diagnostic laser is more likely to be miniaturized for minimally invasive surgery (MIS). In MIS, the laser light should be delivered through an optical fiber (a small bending radius and core size are required) inside the narrow channel of an endoscope, which is not an easy task if the peak energy is high. In addition, since it is not an imaging-based method, unlike OCT, a single optical fiber can be used to collect the data. No scanning part (like MEMS mirror)

is required, thus, less space needs to be dedicated to the detecting system in the endoscope. Moreover, imaging methods are more likely to diminish in performance in-vivo, as increased debris reduces the quality of the image. Compared to spectroscopic methods (LIBS, Raman, DRS, autofluorescence, and random lasing), the spectrometer is not required, and the delivering optical fiber is connected directly to the camera. Thus, the cost of the final setup could be less, without the need for the expensive, high-resolution spectrometer typically used in such setups [83]. Our method does not require a full-frame reading, meaning that the sampling rate (frame per second) can be higher and the time dedicated to signal processing (for classification) is much less in the proposed method. The processing time depends on both, the integration time and the time required for computation. For example, in Raman spectroscopy, where the cross-section of the signal is low, the tissue should be exposed to the light for a long time (e.g., 10 s [14], or 5 s [15]) in order to get the spectra; therefore it can only be applied in a near-real-time scenario. There are few studies that have reported tissue differentiation methods in real-time [41–44]; to the best of our knowledge, all of them have used a single laser for ablation and tissue-type detection. In cases where a single laser is used for both ablation and detection, the diagnostic laser stops together with the ablation laser once the laser reaches a tissue that should be preserved. Therefore, a closed-loop scenario cannot be repeated, meaning that the ablation can start with the tissue that needs to be ablated, and will stop once the laser beam reaches other tissue types, after which, neither ablation nor tissue type detection can be continued.

The main drawback of the proposed method is the absence of tissue differentiation among soft tissues. Most of the other methods have been explored for their ability to differentiate between hard and soft tissues as well as among different soft tissues. Additionally, some tissue properties, like dehydration and carbonization, are detectable through other methods [38,39]. The current method is most useful for surgeries in which the soft tissues must be preserved. It is worth mentioning that the ablation threshold can also be slightly different among similar tissues (e.g., among retinal pigment epithelial (RPE) melanosome, and melanin compared to cutaneous melanosome [84,85]). Note that the threshold is also a function of tissue temperature [86,87]. Therefore, with more stabilized laser energy and deep-cooled detector (and also constant tissue temperature), differentiation between soft tissues could also be possible. However, the current setup has multiple applications, and all green checkmarks in Table 1 can be given to it.

4.2. Outlook

The current system can be improved by integrating the OCT system in the loop, which was conducted offline in this study. As the OCT provides complementary information, both, the information about the type of tissue and information about the depth of cut can be used in a closed-loop system. We also plan to deliver both lasers using a fiber-based system. In this way, the system will be ready to be fitted inside the channel of an endoscope for MIS applications. Currently, only the collection fiber is suitable for an endoscope; the rest of the setup is in free-space. As mentioned above, by employing nanosecond lasers, ablation will be based on photodisruption, whereby all the associated phenomena take place together even at the very threshold. Therefore, one alternative to the current camera-based detection system is to use a microphone to detect whether ablation has occurred or not, based on shockwave detection. Also, a simpler camera or a photomultiplier/photodetector can replace the current ICCD, in order to reduce the final cost of the system. Another possible improvement could be to increase the frequency of diagnostic pulses for more precise tissue border detection than achievable at the current setup of every 250 μ s (it corresponds to every 250 μ m, with 1 mm/s moving speed). In the current setup, a lateral error of maximum $\pm 250 \mu$ m could occur when determining tissue border. Finally, an optimized control of the irrigation system needs to be added to avoid thermal damage to the surrounding tissue [81,82]; for this, the effect of water spray on efficiency of the current system should be investigated.

5. Conclusion

A novel method for differentiating hard from soft tissue was proposed and tested in a closed-loop real-time system. A short overview of other similar methods, together with relevant advantages and disadvantages of each as compared to the proposed method, was provided. We concluded that the proposed method could be less costly, since no spectrometer is required, and that the experiment could be performed with a higher sampling rate (no full-frame recording, no heavy signal processing required). Given that the ablation took place in the hard tissue only, the soft tissue was preserved even after several round trips of the laser beam. Because the proposed method is a non-imaging setup with a low energy pulse, it is very likely to be miniaturized to be fitted inside the narrow channel of an endoscope. The setup, for now, can be used for free-space ablation; however, a future fiber-based setup for MIS is planned. Likewise, an OCT system will be integrated into the current setup for full control of cutting depth and for detecting the type of tissue during surgery, in the real-time.

Funding

Werner Siemens Foundation through the Minimally Invasive Robot-Assisted Computer-guided LaserosteotomyE (MIRACLE) project.

Acknowledgments

The authors gratefully acknowledge the assistance given by Prof. Georg Rauter and his team.

Disclosures

The authors declare no conflicts of interest.

References

1. D. G. Panduric, I. B. Juric, S. Music, K. Molcanov, M. Susic, and I. Anic, "Morphological and ultrastructural comparative analysis of bone tissue after Er:YAG laser and surgical drill osteotomy," *Photomed. Laser Surg.* **32**(7), 401–408 (2014).
2. N. Jowett, W. Wöllmer, R. Reimer, J. Zustin, U. Schumacher, P. W. Wiseman, A. M. Mlynarek, A. Böttcher, C. V. Dalchow, B. B. Lörincz, R. Knecht, and R. J. D. Miller, "Bone Ablation without Thermal or Acoustic Mechanical Injury via a Novel Picosecond Infrared Laser (PIRL)," *Otolaryngol.–Head Neck Surg.* **150**(3), 385–393 (2014).
3. S. Stübinger, "Advances in bone surgery: the Er:YAG laser in oral surgery and implant dentistry," *Clin., Cosmet. Invest. Dent.* **2**, 47–62 (2010).
4. Y.-M. Lee, R. Y. Tu, A. Chiang, and Y.-C. Huang, "Average-power mediated ultrafast laser osteotomy using a mode-locked Nd:YVO4 laser oscillator," *J. Biomed. Opt.* **12**(6), 060505 (2007).
5. B. Girard, K. Franjic, M. Cloutier, D. Wilson, C. M. L. Cloke, B. C. Wilson, and R. J. Dwayne Miller, *Bone surgery with femtosecond laser compared to mechanical instruments: healing studies*, High-Power Laser Ablation 2006 (SPIE, 2006), Vol. 6261.
6. M. Ivanenko, M. Werner, S. Afilal, M. Klasing, and P. Hering, "Ablation of hard bone tissue with pulsed CO2 lasers," *Med. Laser Appl.* **20**(1), 13–23 (2005).
7. L. Beltrán, H. Abbasi, G. Rauter, N. Friederich, P. Cattin, and A. Zam, *Effect of laser pulse duration on ablation efficiency of hard bone in microseconds regime*, Third International Conference on Applications of Optics and Photonics (SPIE, 2017), Vol. 10453.
8. H. Abbasi, L. Beltrán, G. Rauter, R. Guzman, P. C. Cattin, and A. Zam, *Effect of cooling water on ablation in Er:YAG laserosteotomy of hard bone*, Third International Conference on Applications of Optics and Photonics (SPIE, 2017), Vol. 10453.
9. R. Mauceri, V. Panzarella, L. Maniscalco, A. Bedogni, M. E. Licata, A. Albanese, F. Toia, E. M. G. Cumbo, G. Mazzola, O. Di Fede, and G. Campisi, "Conservative Surgical Treatment of Bisphosphonate-Related Osteonecrosis of the Jaw with Er:Cr:YSGG Laser and Platelet-Rich Plasma: A Longitudinal Study," *BioMed Res. Int.* **2018**, 1–10 (2018).
10. Y. Ohsugi, A. Aoki, K. Mizutani, S. Katagiri, M. Komaki, M. Noda, T. Takagi, S. Kakizaki, W. Meinzer, and Y. Izumi, "Evaluation of bone healing following Er:YAG laser ablation in rat calvaria compared with bur drilling," *J. Biophotonics* **12**(3), e201800245 (2019).
11. M. Augello, C. Baetscher, M. Segesser, H.-F. Zeilhofer, P. Cattin, and P. Juergens, "Performing partial mandibular resection, fibula free flap reconstruction and midfacial osteotomies with a cold ablation and robot-guided Er:YAG

- laser osteotome (CARLO®) – A study on applicability and effectiveness in human cadavers,” *J. Cranio Maxill Surg.* **46**(10), 1850–1855 (2018).
12. Y. A. Bayhaqi, A. Navarini, G. Rauter, P. C. Cattin, and A. Zam, *Neural network in tissue characterization of Optical Coherence Tomography (OCT) image for smart laser surgery: preliminary study*, Third International Seminar on Photonics, Optics, and Its Applications (ISPhOA 2018) (SPIE, 2019), Vol. 11044.
 13. Y. A. Bayhaqi, G. Router, A. Navarini, P. C. Cattin, and A. Zam, *Fast optical coherence tomography image enhancement using deep learning for smart laser surgery: preliminary study in bone tissue*, IV International Conference on Applications of Optics and Photonics (AOP 2019) (SPIE, 2019), Vol. 11207.
 14. T. Minamikawa, Y. Harada, and T. Takamatsu, *Raman spectroscopic detection of peripheral nerves towards nerve-sparing surgery*, SPIE BiOS (SPIE, 2017), Vol. 10054.
 15. L. A. Reisner, B. W. King, M. D. Klein, G. W. Auner, and A. K. Pandya, “A prototype biosensor-integrated image-guided surgery system,” *Int. J. Med. Robotics Comput. Assist. Surg.* **3**(1), 82–88 (2007).
 16. P. C. Ashok, N. Krstajić, M. E. Giardini, K. Dholakia, and W. Sibbett, “Raman Spectroscopy Sensor for Surgical Robotics – Instrumentation and Tissue Differentiation Algorithm,” in *Biomedical Optics and 3-D Imaging*, OSA Technical Digest (Optical Society of America, 2012), JM3A.26.
 17. P. C. Ashok, M. E. Giardini, K. Dholakia, and W. Sibbett, “A Raman spectroscopy bio-sensor for tissue discrimination in surgical robotics,” *J. Biophotonics* **7**(1-2), 103–109 (2014).
 18. F. Stelzle, C. Knipfer, W. Adler, M. Rohde, N. Oetter, E. Nkenke, M. Schmidt, and K. Tangermann-Gerk, “Tissue Discrimination by Uncorrected Autofluorescence Spectra: A Proof-of-Principle Study for Tissue-Specific Laser Surgery,” *Sensors* **13**(10), 13717–13731 (2013).
 19. A. Zam, “Optical Tissue Differentiation for Sensor-Controlled Tissue-Specific Laser Surgery,” (2011).
 20. R. Gunaratne, I. Monteath, J. Goncalves, R. Sheh, C. N. Ironside, M. Kapfer, R. Chipper, B. Robertson, R. Khan, and D. Fick, “Machine learning classification of human joint tissue from diffuse reflectance spectroscopy data,” *Biomed. Opt. Express* **10**(8), 3889–3898 (2019).
 21. A. Zam, F. Stelzle, K. Tangermann-Gerk, W. Adler, E. Nkenke, F. W. Neukam, M. Schmidt, and A. Douplik, “In vivo soft tissue differentiation by diffuse reflectance spectroscopy: preliminary results,” *Phys. Procedia* **5**, 655–658 (2010).
 22. F. Stelzle, A. Zam, W. Adler, K. Tangermann-Gerk, A. Douplik, E. Nkenke, and M. Schmidt, “Optical Nerve Detection by Diffuse Reflectance Spectroscopy for Feedback Controlled Oral and Maxillofacial Laser Surgery,” *J. Transl. Med.* **9**(1), 20 (2011).
 23. F. Stelzle, K. Tangermann-Gerk, W. Adler, A. Zam, M. Schmidt, A. Douplik, and E. Nkenke, “Diffuse reflectance spectroscopy for optical soft tissue differentiation as remote feedback control for tissue-specific laser surgery,” *Lasers Surg. Med.* **42**(4), 319–325 (2010).
 24. B. Lengenfelder, K. Schwarzkopf, N. Oetter, F. Mehari, E. Eschner, F. Klämpfl, F. Stelzle, M. Kesting, Z. Zalevsky, and M. Schmidt, *Acoustic differentiation of dental soft and hard tissues using remote speckle-analysis during Er:YAG ablation*, European Conferences on Biomedical Optics (SPIE, 2019), Vol. 11077.
 25. B. Lengenfelder, F. Mehari, M. Hohmann, M. Heinlein, E. Chelales, M. J. Waldner, F. Klämpfl, Z. Zalevsky, and M. Schmidt, “Remote photoacoustic sensing using speckle-analysis,” *Sci. Rep.* **9**(1), 1057 (2019).
 26. B. Lengenfelder, F. Mehari, M. Hohmann, C. Löhr, M. J. Waldner, M. Schmidt, Z. Zalevsky, and F. Klämpfl, “Contact-free endoscopic photoacoustic sensing using speckle-analysis,” *J. Biophotonics* **12**(12), e201900130 (2019).
 27. H. N. Kenhagho, G. Rauter, R. Guzman, P. Cattin, and A. Zam, “Optoacoustic Tissue Differentiation Using a Mach-Zehnder Interferometer: Preliminary Results,” in *2018 IEEE International Ultrasonics Symposium (IUS)*, 2018), 1–9.
 28. H. N. Kenhagho, G. Rauter, R. Guzman, P. C. Cattin, and A. Zam, “Optoacoustic Tissue Differentiation Using a Mach-Zehnder Interferometer,” *IEEE Trans. Ultrason., Ferroelect., Freq. Contr.* **66**(9), 1435–1443 (2019).
 29. H. Nguendon Kenhagho, S. Shevchik, F. Saeidi, N. Faivre, B. Meylan, G. Rauter, R. Guzman, P. Cattin, K. Wasmer, and A. Zam, “Characterization of Ablated Bone and Muscle for Long-Pulsed Laser Ablation in Dry and Wet Conditions,” *Materials* **12**(8), 1338 (2019).
 30. M. Hohmann, D. Dörner, F. Mehari, C. Chen, M. Späth, S. Müller, H. Albrecht, F. Klämpfl, and M. Schmidt, “Investigation of random lasing as a feedback mechanism for tissue differentiation during laser surgery,” *Biomed. Opt. Express* **10**(2), 807–816 (2019).
 31. H. Abbasi, G. Rauter, R. Guzman, P. C. Cattin, and A. Zam, *Differentiation of femur bone from surrounding soft tissue using laser-induced breakdown spectroscopy as a feedback system for smart laserosteotomy*, SPIE Photonics Europe (SPIE, 2018), Vol. 10685.
 32. R. Kanawade, F. Mehari, C. Knipfer, M. Rohde, K. Tangermann-Gerk, M. Schmidt, and F. Stelzle, “Pilot study of laser induced breakdown spectroscopy for tissue differentiation by monitoring the plume created during laser surgery — An approach on a feedback Laser control mechanism,” *Spectrochim. Acta, Part B* **87**, 175–181 (2013).
 33. R. Kanawade, F. Mahari, F. Klämpfl, M. Rohde, C. Knipfer, K. Tangermann-Gerk, W. Adler, M. Schmidt, and F. Stelzle, “Qualitative tissue differentiation by analysing the intensity ratios of atomic emission lines using laser induced breakdown spectroscopy (LIBS): prospects for a feedback mechanism for surgical laser systems,” *J. Biophotonics* **8**(1-2), 153–161 (2015).
 34. F. Mehari, M. Rohde, C. Knipfer, R. Kanawade, F. Klämpfl, W. Adler, F. Stelzle, and M. Schmidt, “Laser induced breakdown spectroscopy for bone and cartilage differentiation - ex vivo study as a prospect for a laser surgery feedback mechanism,” *Biomed. Opt. Express* **5**(11), 4013–4023 (2014).

35. F. Mehari, M. Rohde, R. Kanawade, C. Knipfer, W. Adler, F. Klämpfl, F. Stelzle, and M. Schmidt, "Investigation of the differentiation of ex vivo nerve and fat tissues using laser-induced breakdown spectroscopy (LIBS): Prospects for tissue-specific laser surgery," *J. Biophotonics* **9**(10), 1021–1032 (2016).
36. M. Rohde, F. Mehari, F. Klämpfl, W. Adler, F.-W. Neukam, M. Schmidt, and F. Stelzle, "The differentiation of oral soft- and hard tissues using laser induced breakdown spectroscopy – a prospect for tissue specific laser surgery," *J. Biophotonics* **10**(10), 1250–1261 (2017).
37. X. Li, S. Yang, R. Fan, X. Yu, and D. Chen, "Discrimination of soft tissues using laser-induced breakdown spectroscopy in combination with k nearest neighbors (kNN) and support vector machine (SVM) classifiers," *Opt. Laser Technol.* **102**, 233–239 (2018).
38. H. Abbasi, G. Rauter, R. Guzman, P. C. Cattin, and A. Zam, "Laser-induced breakdown spectroscopy as a potential tool for autocoagulation detection in laserosteotomy," *J. Biomed. Opt.* **23**(7), 1–7 (2018).
39. H. Abbasi, I. Sugiarto, G. Rauter, R. Guzman, P. C. Cattin, and A. Zam, "Pilot Ex Vivo Study of Laser-Induced Breakdown Spectroscopy to Detect Bone Dehydration: An Approach for Irrigation Feedback in Laserosteotomy," in *International Conference on Electrical Engineering & Computer Science (ICEECS 2018)*, (Bali, Indonesia, 2018).
40. F. Mehari, B. Lengenfelder, R. Figura, F. Klämpfl, and M. Schmidt, "LIBS based Tissue Differentiation for Er: YAG Surgical Laser," *Proceedings of the 6th International Conference on Photonics, Optics and Laser Technology - Volume 1: PHOTOPTICS*, 5 (2018).
41. K. Henn, G. G. Gubaidullin, J. Bongartz, J. Wahrburg, H. Roth, and M. Kunkel, "A spectroscopic approach to monitor the cut processing in pulsed laser osteotomy," *Lasers Med. Sci.* **28**(1), 87–92 (2013).
42. H. Huang, L.-M. Yang, S. Bai, and J. Liu, "Smart surgical tool," *J. Biomed. Opt.* **20**(07), 1–7 (2015).
43. S. Rupprecht, K. Tangermann, P. Kessler, F. W. Neukam, and J. Wiltfang, "Er:YAG laser osteotomy directed by sensor controlled systems," *J. Cranio Maxill Surg.* **31**(6), 337–342 (2003).
44. S. Rupprecht, K. Tangermann-Gerk, J. Wiltfang, F. W. Neukam, and A. Schlegel, "Sensor-based laser ablation for tissue specific cutting: an experimental study," *Lasers Med. Sci.* **19**(2), 81–88 (2004).
45. A. Seifalinezhad, M. Bahreini, M. M. Hassani Matin, and S. H. Tavassoli, "Feasibility Study on Discrimination of Neo-plastic and Non-Neoplastic Gastric Tissues Using Spark Discharge Assisted Laser Induced Breakdown Spectroscopy," *J. Lasers Med. Sci.* **10**(1), 64–69 (2018).
46. J. H. Han, Y. Moon, J. J. Lee, S. Choi, Y.-C. Kim, and S. Jeong, "Differentiation of cutaneous melanoma from surrounding skin using laser-induced breakdown spectroscopy," *Biomed. Opt. Express* **7**(1), 57–66 (2016).
47. Y. Moon, J. H. Han, S. Shin, Y.-C. Kim, and S. Jeong, "Elemental analysis of tissue pellets for the differentiation of epidermal lesion and normal skin by laser-induced breakdown spectroscopy," *Biomed. Opt. Express* **7**(5), 1626–1636 (2016).
48. X. Chen, X. Li, S. Yang, X. Yu, and A. Liu, "Discrimination of lymphoma using laser-induced breakdown spectroscopy conducted on whole blood samples," *Biomed. Opt. Express* **9**(3), 1057–1068 (2018).
49. A. V. DSouza, H. Lin, E. R. Henderson, K. S. Samkoe, and B. W. Pogue, "Review of fluorescence guided surgery systems: identification of key performance capabilities beyond indocyanine green imaging," *J. Biomed. Opt.* **21**(8), 080901 (2016).
50. A. L. Lazarides, M. J. Whitley, D. B. Strasfeld, D. M. Cardona, J. M. Ferrer, J. L. Mueller, H. L. Fu, S. Bartholf DeWitt, B. E. Brigman, N. Ramanujam, D. G. Kirsch, and W. C. Eward, "A Fluorescence-Guided Laser Ablation System for Removal of Residual Cancer in a Mouse Model of Soft Tissue Sarcoma," *Theranostics* **6**(2), 155–166 (2016).
51. J. Odenthal, P. Friedl, and R. P. Takes, "Compatibility of CO₂ laser surgery and fluorescence detection in head and neck cancer cells," *Head & Neck* **41**(5), 1253–1259 (2019).
52. S. R. Visuri, J. T. Walsh Jr., and H. A. Wigdor, "Erbium laser ablation of dental hard tissue: Effect of water cooling," *Lasers Surg. Med.* **18**(3), 294–300 (1996).
53. M. Papadaki, A. Doukas, W. A. Farinelli, L. Kaban, and M. Troulis, "Vertical ramus osteotomy with Er:YAG laser: a feasibility study," *Int. J. Oral Maxillofac. Surg.* **36**(12), 1193–1197 (2007).
54. L. Kuscer and J. Diaci, "Measurements of erbium laser-ablation efficiency in hard dental tissues under different water cooling conditions," *J. Biomed. Opt.* **18**(10), 108002 (2013).
55. V. Tuchin, "Tissue optics and photonics: Light-tissue interaction II," *J. Biomed. Photonics Eng.* **2**(3), 030201 (2016).
56. N. M. Fried and D. Fried, "Comparison of Er:YAG and 9.6- μ m TE CO₂ lasers for ablation of skull tissue," *Lasers Surg. Med.* **28**(4), 335–343 (2001).
57. N. Fried and D. Fried, *Laser ablation of skull tissue using transverse excited 9.6-um CO₂ lasers with pulse durations of 1-100 us*, BiOS 2000 The International Symposium on Biomedical Optics (SPIE, 2000), Vol. 3914.
58. K. Chan, N. Fried, and D. Fried, *Selective ablation of carious lesions using an integrated multispectral near-IR imaging system and a novel 9.3-um CO₂ laser*, SPIE BiOS (SPIE, 2018), Vol. 10473.
59. A. Charlton, M. R. Dickinson, T. A. King, and A. J. Freemont, "Erbium-YAG and holmium-YAG laser ablation of bone," *Lasers Med. Sci.* **5**(4), 365–373 (1990).
60. M. Buchelt, H.-P. Kutschera, T. Katterschafka, H. Kiss, S. Lang, R. Beer, and U. Losert, "Erb:YAG and Hol:YAG Laser Osteotomy: The Effect of Laser Ablation on Bone Healing," *Lasers Surg. Med.* **15**(4), 373–381 (1994).
61. J. T. Walsh Jr. and T. F. Deutsch, "Er:YAG laser ablation of tissue: Measurement of ablation rates," *Lasers Surg. Med.* **9**(4), 327–337 (1989).

62. A. Vogel and V. Venugopalan, "Mechanisms of Pulsed Laser Ablation of Biological Tissues," *Chem. Rev.* **103**(2), 577–644 (2003).
63. J. Noack, D. X. Hammer, G. D. Noojin, B. A. Rockwell, and A. Vogel, "Influence of pulse duration on mechanical effects after laser-induced breakdown in water," *J. Appl. Phys.* **83**(12), 7488–7495 (1998).
64. N. Linz, S. Freidank, X.-X. Liang, and A. Vogel, "Wavelength dependence of femtosecond laser-induced breakdown in water and implications for laser surgery," *Phys. Rev. B* **94**(2), 024113 (2016).
65. A. Vogel, "Nonlinear absorption: intraocular microsurgery and laser lithotripsy," *Phys. Med. Biol.* **42**(5), 895–912 (1997).
66. J.-L. Boulnois, "Photophysical processes in recent medical laser developments: A review," *Lasers Med. Sci.* **1**(1), 47–66 (1986).
67. F. Reza, K. A. Katayoun, A. Farzaneh, and T. Nikoo, "Laser in orthodontics," in *Principles in Contemporary Orthodontics* (IntechOpen, 2011).
68. Z. Qin and J. C. Bischof, "Thermophysical and biological responses of gold nanoparticle laser heating," *Chem. Soc. Rev.* **41**(3), 1191–1217 (2012).
69. M. H. Niemz, *Laser-tissue interactions* (Springer, 2007).
70. S. L. Jacques, "Laser-Tissue Interactions: Photochemical, Photothermal, and Photomechanical," *Surg. Clin. North Am.* **72**(3), 531–558 (1992).
71. A. Vogel, W. Lauterborn, and R. Timm, "Optical and acoustic investigations of the dynamics of laser-produced cavitation bubbles near a solid boundary," *J. Fluid Mech.* **206**, 299–338 (1989).
72. A. Vogel, S. Busch, K. Jungnickel, and R. Birngruber, "Mechanisms of intraocular photodisruption with picosecond and nanosecond laser pulses," *Lasers Surg. Med.* **15**(1), 32–43 (1994).
73. R. O. Esenaliev, A. A. Oraevsky, S. L. Jacques, and F. K. Tittel, *Effect of tensile stress amplitude and temporal characteristics on threshold of cavitation-driven ablation*, Photonics West '96 (SPIE, 1996), Vol. 2681.
74. S. L. Jacques, *How tissue optics affect dosimetry for photochemical, photothermal, and photomechanical mechanisms of laser-tissue interaction*, Recent Advances in the Uses of Light in Physics, Chemistry, Engineering, and Medicine (SPIE, 1992), Vol. 1599.
75. A. Vogel and V. Venugopalan, "Pulsed laser ablation of soft biological tissues," in *Optical-Thermal Response of Laser-Irradiated Tissue* (Springer, 2010), pp. 551–615.
76. A. Gholami, M. Baradaran-Ghahfarokhi, M. Ebrahimi, and M. Baradaran-Ghahfarokhi, "Thermal effects of laser-osteotomy on bone: mathematical computation using maple," *J. Med. Signals Sens.* **3**(4), 262 (2013).
77. Y. Suzuki and A. Tachibana, "Measurement of the μm sized radius of Gaussian laser beam using the scanning knife-edge," *Appl. Opt.* **14**(12), 2809–2810 (1975).
78. I. Standard, "11146," "Test methods for laser beam widths, divergence angles and beam propagation ratios"(2005)."
79. M. Nazeri, A. E. Majid, R. Massudi, S. H. Tavassoli, A. Mesbahinia, and H. Abbasi, "Laser-Induced Breakdown Spectroscopy Via the Spatially Resolved Technique Using Non-Gated Detector," *J. Russ. Laser Res.* **37**(2), 164–171 (2016).
80. H. Abbasi, G. Rauter, R. Guzman, P. C. Cattin, and A. Zam, *Plasma plume expansion dynamics in nanosecond Nd:YAG laserosteotome*, SPIE BiOS (SPIE, 2018), Vol. 10505.
81. L. M. B. Bernal, G. Shayeganrad, G. Kosa, M. Zelechowski, G. Rauter, N. Friederich, P. C. Cattin, and A. Zam, *Performance of Er:YAG laser ablation of hard bone under different irrigation water cooling conditions*, SPIE BiOS (SPIE, 2018), Vol. 10492.
82. M. Beltran Bernal Lina, T. Schmidt Iris, N. Vulin, J. Widmer, G. Snedeker Jess, C. Cattin Philippe, A. Zam, and G. Rauter, "Optimizing controlled laser cutting of hard tissue (bone)," in *at - Automatisierungstechnik*, (2018), p. 1072.
83. H. Abbasi, G. Rauter, R. Guzman, P. C. Cattin, and A. Zam, *Design and implementation of a compact high-throughput echelle spectrometer using off-the-shelf off-axis parabolic mirrors for analysis of biological samples by LIBS (Conference Presentation)*, SPIE Optical Metrology (SPIE, 2019), Vol. 11060.
84. S. L. Jacques, R. D. Glickman, and J. A. Schwartz, *Internal absorption coefficient and threshold for pulsed laser disruption of melanosomes isolated from retinal pigment epithelium*, Photonics West '96 (SPIE, 1996), Vol. 2681.
85. S. L. Jacques, A. A. Oraevsky, C. R. Thompson, and B. S. Gerstman, *Working theory and experiments on photomechanical disruption of melanosomes to explain the threshold for minimal visible retinal lesions for sub-ns laser pulses*, OE/LASE '94 (SPIE, 1994), Vol. 2134.
86. S. L. Jacques and D. J. McAuliffe, "The melanosome: threshold temperature for explosive vaporization and internal absorption coefficient during pulsed laser irradiation," *Photochem. Photobiol.* **53**(6), 769–775 (1991).
87. S. L. Jacques, "Optical properties of biological tissues: a review," *Phys. Med. Biol.* **58**(11), R37–R61 (2013).